ROYAL SOCIETY
OF CHEMISTRY

PAPER

Check for updates

Anomalous wrinkle propagation in polycrystalline graphene with tilt grain boundaries

Zihui Zhao,†[ab] Yafei Wang†[c] and Changguo Wang ⓘ *[ab]

Understanding the propagation of dynamic wrinkles in polycrystalline graphene with grain boundaries (GBs) is critical to the practical application of graphene-based nanodevices. Although wrinkle propagation behavior in pristine graphene (PG) and some defect-containing graphene samples have been investigated, there are no studies on the dynamic behavior of graphene with tilt GBs. Here, nine tilt GBs are constructed in graphene, and molecular dynamics (MD) simulations are performed to investigate anomalous wrinkle propagation. The MD simulation results show that a larger misorientation angle α first enhances the shielding effect of tilt GBs on wrinkle propagation before it weakens. The maximum Δz root mean square (RMS) shows that a greater misorientation angle α first increases the maximum RMS of the GB region (R_{GB}) before it then decreases, while the maximum RMS of R_{80} exhibits the opposite trend. Moreover, approximately 96% of the C_{60} kinetic energy is converted into kinetic and potential energies in graphene, and the potential energy in graphene presents two evolution modes. Phase diagrams are plotted to study the effect of the distance d_1 and rotation angle β on the wrinkle propagation and sensitivity of the maximum RMS value to d_1. It is expected that our results can provide a fundamental understanding of defect engineering and guidelines to design protectors, energy absorbers, and defect detectors in nanodevices.

1. Introduction

Graphene is a well-known two-dimensional (2D) material, composed of a hexagonal structure of carbon atoms, that has attracted significant attention since its discovery.[1] Graphene has exhibited extraordinary capabilities in widespread applications, due to its exceptional mechanical,[2–4] electronic,[5,6] thermal,[7–9] and magnetic properties.[10,11] In addition, graphene is an important material that can be used in shock absorption equipment due to its extraordinary stiffness, strength and elasticity. Thus, studying its impact dynamics is significant in various applications, such as sensors, actuators and nanofiltration membranes.[12] The impact dynamic mechanical behavior of graphene has been studied intensively, especially for dynamic wrinkle propagation and the ballistic performance of graphene.[12–17] Moreover, extensive studies have been conducted to investigate dynamic wrinkle propagation, such as anisotropic

wave propagation,[18,19] transverse wave propagation,[19–21] buckling-driven wrinkles,[22–25] and dynamic ripple pattern regulation[26,27] in graphene. With the development of synthetic processes, the production of large-area graphene can be realized *via* chemical vapor deposition (CVD),[28,29] thermal graphitization,[30] and liquid-phase exfoliation.[31] Hence, graphene is considered a promising candidate for a large spectrum of devices, such as nanoelectro-mechanical systems (NEMS), sensors, and ultrasensitive detection.[32–34] However, various defects, especially grain boundaries (GBs), inevitably exist intrinsically during the mass production of graphene.[35,36] Generally, defects and GBs in graphene are undesirable as they may degrade the device performance. For instance, the mechanical properties and carrier mobilities of graphene can be affected by point defects and GBs.[37–39] In addition, the graphene strength can be reduced significantly from GBs with smaller misorientation angles.[40]

Despite the undesirable effect of defects on the properties of graphene, defect engineering plays a crucial role in adjusting the graphene properties, such as opening a band gap,[41] selective molecular sieving through graphene nanopores,[42] tuning the mechanical and material properties,[43,44] and regulating the thermal conductivity.[45,46] For example, Sun *et al.*[42] studied gas transport through individual graphene pores created from low intensity exposure to low kV electrons and obtained the long-sought-after exponential selectivity through angstrom-scale pores in 2D membranes. Zheng *et al.*[43] investigated the

a National Key Laboratory of Science and Technology on Advanced Composites in Special Environments, Harbin Institute of Technology, Harbin 150080, China. E-mail: wangcg@hit.edu.cn

b Center for Composite Materials and Structures, Harbin Institute of Technology, Harbin 150001, China

c Institute of Mechanics and Computational Engineering, Department of Aeronautics and Astronautics, Fudan University, 220 Handan Road, Shanghai 200433, China

† These authors contributed equally to this work.

This journal is © the Owner Societies 2023

Phys. Chem. Chem. Phys., 2023, **25**, 3681–3694 | **3681**

tunability of graphene mechanical anisotropy through the design of defect engineering and found the ability to tune the mechanical properties in different directions through defect designs. Sun et al.[45] studied the effect of GBs and grain size on the thermal transport of special penta-graphene using non-equilibrium molecular dynamics (MD) simulations, and provided effective strategies to modulate the thermal conductivity *via* the defect engineering of 2D materials. As an important role of defect engineering, GBs are expected to be used in more extensive applications, such as the adsorption and diffusion of sodium in ion batteries,[47] the modulation of wrinkling in graphene,[48] and the regulation of structures and electronic spectra of graphene layers with tilt GBs.[49]

Previous researchers focused primarily on the effects of GBs on the static mechanical properties of graphene, and little attention has been given to the dynamic mechanical properties of polycrystalline graphene, especially out-of-plane dynamic deformation. However, graphene-based devices, such as sensors and ultrasensitive devices,[33,34] are prone to the influence of nanoparticle impacts, and the failure of precision devices can be attributed to dynamic wrinkles brought about by impacts. Therefore, shielding for dynamic wrinkles based on defect engineering designs is vital for the practical application of nanodevices. Recently, the effect of defects and GBs on dynamic wrinkle propagation in graphene was investigated *via* MD simulations, and the capability of absorbing and storing energy from dynamic wrinkles was obtained.[14,19,50] However, the influence of the dynamic wrinkle propagation from tilt GBs in polycrystalline graphene remains unclear. In addition, as common GBs in defect engineering, tilt GBs usually exhibit counterintuitive mechanical properties.[51–53] Graphene sheets with large misorientation angle tilt GBs are much stronger than those with low misorientation angle tilt GBs, which is counter to standard reasoning. Therefore, a natural question is whether or not the counterintuitive influence of tilt GBs still holds true for the propagation of dynamic wrinkles. This study employs MD simulations to systematically study dynamic wrinkle propagation in graphene with a series of tilt GBs to better understand their effect.

This paper is organized as follows. Section 2 provides the construction of the MD simulation model for graphene with nine tilt GBs and illustrates the simulation methodology. In Section 3, dynamic wrinkle propagation through tilt GBs (Section 3.1), and the influence of the distance d_1 (Section 3.2) and rotation angle β (Section 3.3) on wrinkle propagation are investigated. Section 4 summarizes our results and provides concluding remarks.

2. Models and methods

2.1. Molecular dynamics models of tilt GBs

Graphene sheets with various tilt GBs are constructed under the guidelines presented in ref. 54 As shown in Fig. 1a, a graphene tilt GB consists of two pristine graphene (PG) grains with a misorientation angle α. The angle β represents the rotation angle of a graphene sheet with a tilt GB (Fig. 1b). Nine tilt GB configurations are plotted with misorientation angles α ranging from 1.2° to 21.8° (from left to right in Fig. 1c, α is 1.2, 2.1, 3.8, 5.0, 6.0, 7.3, 9.4, 13.2, and 21.8°). A tilt GB features a periodic line of disclination dipoles, which are composed of five- and seven-membered ring defects (5–7 defects). As shown in Fig. 1c, an increased misorientation angle α causes the number of 5–7 defects to increase and the number of hexagonal rings among the adjacent 5–7 defects to decrease. The distances of the adjacent 5–7 defects in the constructed tilt GBs are approximately 112, 62, 31, 22, 18, 14, 10, 6, and 2 Å. To contain enough 5–7 defects along the tilt GBs and ensure the computation efficiency, the constructed rectangular graphene sheets are sized at around 300 Å (zigzag direction) × 200 Å (armchair direction) in all simulations. Correspondingly, as illustrated in Fig. 1c, the number (N) of 5–7 defects in the simulation models is 1, 3, 5, 7, 9, 11, 13, 19, and 31, respectively.

2.2. Methodology

All atomistic simulations are conducted using the large-scale atomic molecular massively parallel simulator (LAMMPS) program.[55] The adaptive intermolecular reactive empirical bond order (AIREBO) potential[56] is adopted to model the interactions between carbon atoms. The thickness of a graphene monolayer is taken as 3.35 Å,[54] and a 10 Å initial vertical gap is set between the C_{60} molecule and graphene. The radius of the C_{60} molecule is 0.358 nm.[12] A PG and a graphene sheet with a GB can be flat when subjected to in-plane tension.[54,57,58] The PG is considered as suspended and flat in our simulations to neglect the effect of out-of-plane thermal fluctuations and more clearly demonstrate the patterns.[59] The simulation time step is set as 1 fs during the simulations. For defective graphene sheets (*i.e.*, graphene sheets that contain defects) with tilt GBs, all systems are relaxed in the micro-canonical (NVE) ensemble for 0.3 ps while fixing the z-direction displacement of all carbon atoms, which ensures the approximate maximum out-of-plane displacement for atom-a (see Fig. 4). This relaxation strategy provides a unified standard to compare the results between defective graphene and PG. Then, impact simulations are performed with NVE ensembles for 10 ps to conserve energy. An initial temperature of 5 K is assigned to the graphene sheet. The C_{60} molecule moves towards graphene at an initial velocity of 15 Å ps^{-1}. Periodic boundary conditions are used in MD simulations. During the impact phase, all four edges of the rectangular graphene sheets are perfectly clamped with a width of 5 Å, and a Berendsen thermal bath is utilized to control the temperature of the graphene sheets.

3. Results and discussion

3.1. Wrinkle propagation through tilt GBs

In previous studies, the out-of-plane displacement of special atoms and snapshots of MD simulations for PG and defective graphene are presented to study the evolution of dynamic wrinkle propagation, which are proved to be valid.[14–16,50] To investigate the evolution of dynamic wrinkle propagation
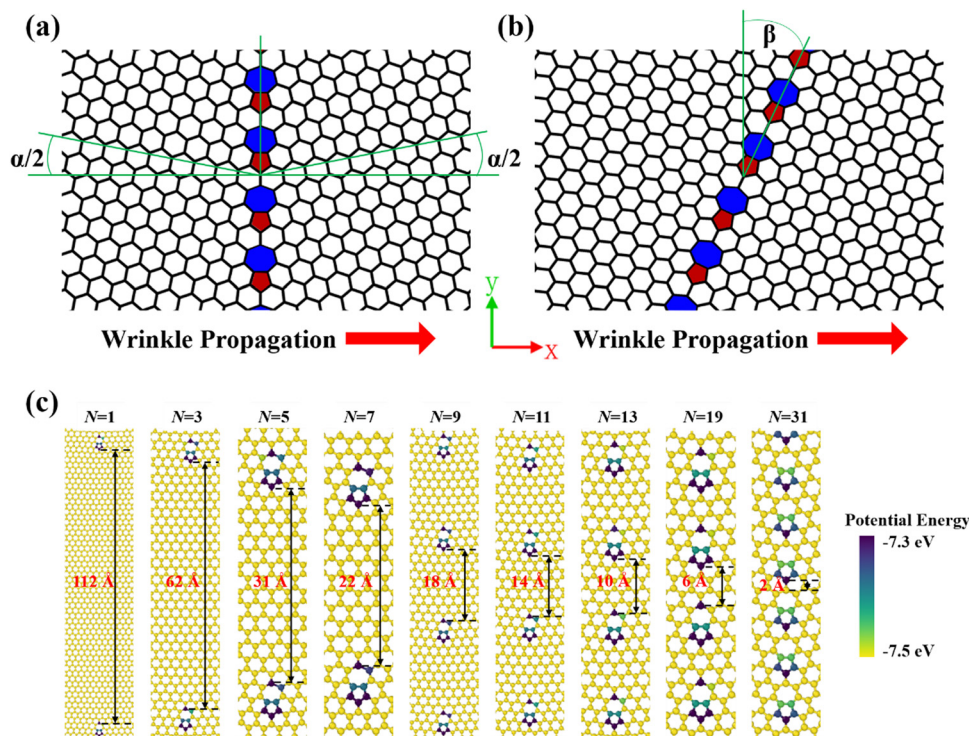
3682 | *Phys. Chem. Chem. Phys.*, 2023, **25**, 3681–3694

This journal is © the Owner Societies 2023

Fig. 1 Schematic illustration of tilt GBs in graphene and plots of the tilt GB configurations. (a) The misorientation angle α between two PG grains, (b) the rotation angle β of a graphene sheet with a tilt GB, and (c) the atomic configurations of various constructed tilt GBs with misorientation angles α ranging from 1.2° to 21.8° (1.2, 2.1, 3.8, 5.0, 6.0, 7.3, 9.4, 13.2, and 21.8° from left to right). N denotes the number of 5–7 defects in the constructed simulation models, and the units of potential energy are in eV. Atoms are color coded based on their potential energies with dark purple mapped to the maximum and yellow mapped to the minimum.

in graphene with tilt GBs, seven carbon atoms (atom-a, atom-b, atom-c, atom-d, atom-e, atom-f, and atom-g), one atomic line (L_{GB}) and two atomic regions (R_{GB} and R_{80}) are marked in Fig. 2. Taking the $\alpha(1.2)$ GB (*i.e.*, misorientation angle $\alpha = 1.2°$) as an example, the center of the graphene sheet is considered as the origin O. In the simulations, the middle 5–7 defect of GB is constructed at $Y = 0$. A C_{60} molecule impacts the center of the

Fig. 2 Schematic of a graphene sheet with the $\alpha(1.2)$ GB for the dynamic wrinkle propagation calculations. The impact point of the C_{60} molecule is at the center of the graphene sheet, which is considered the origin O. The distance between atom-a and the origin O is approximately 20 Å, and adjacent distances between the seven atoms (atom-a to atom-g) are all about 10 Å. L_{GB} is the atomic line through the 5–7 defects. The R_{GB} denotes the GB region and R_{80} is the single hexagonal ring atomic region. The distances from the origin O to R_{GB} and R_{80} are 30 and 80 Å, respectively.

graphene sheet to observe the symmetric evolution morphology of dynamic wrinkle propagation (see Fig. 3). The distances between the origin O and the seven atoms are approximately 20 Å (atom-a), 30 Å (atom-b), 40 Å (atom-c), 50 Å (atom-d), 60 Å (atom-e), 70 Å (atom-f), and 80 Å (atom-g). As marked in Fig. 2, atom-a is on the left of the GB, and the evolution of its out-of-plane displacement is used to determine the relaxation time. Then, atom-b is the joint atom of the 5–7 defect, which is utilized to study the mechanism of anomalous wrinkle propagation. The other atoms located on the right of the GB are used to investigate the effects of the tilt GB on the dynamic wrinkles. L_{GB} represents the atomic line through the entire tilt GB. The distance d_1 between the origin O and L_{GB} is 30 Å. The evolution of the out-of-plane configurations for the tilt GBs can be measured *via* the L_{GB}. The R_{GB} is the atomic region where all 5–7 defects are contained, and R_{80} is a single hexagonal ring atomic region with a distance between the origin O and R_{80} of 80 Å (*i.e.*, $d_2 = 50$ Å). These two regions are selected to calculate the root mean square (RMS) of the out-of-plane displacement (see Fig. 6a–c). The RMS can be used to study the effect of tilt GBs on dynamic wrinkle propagation.

To intuitively understand the dynamic wrinkle propagation in graphene with tilt GBs, MD simulations are executed to obtain the out-of-plane displacement field of the graphene sheets, as shown in Fig. 3. The simulation results of graphene with five GBs ($\alpha(1.2)$ GB, $\alpha(3.8)$ GB, $\alpha(6.0)$ GB, $\alpha(13.2)$ GB, and
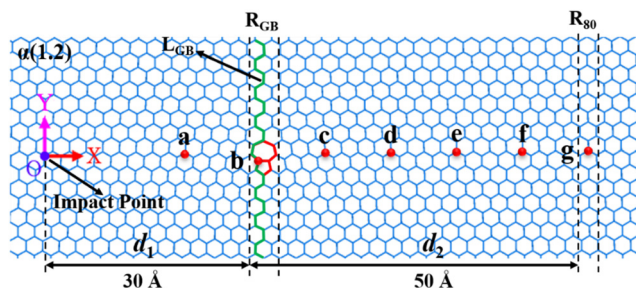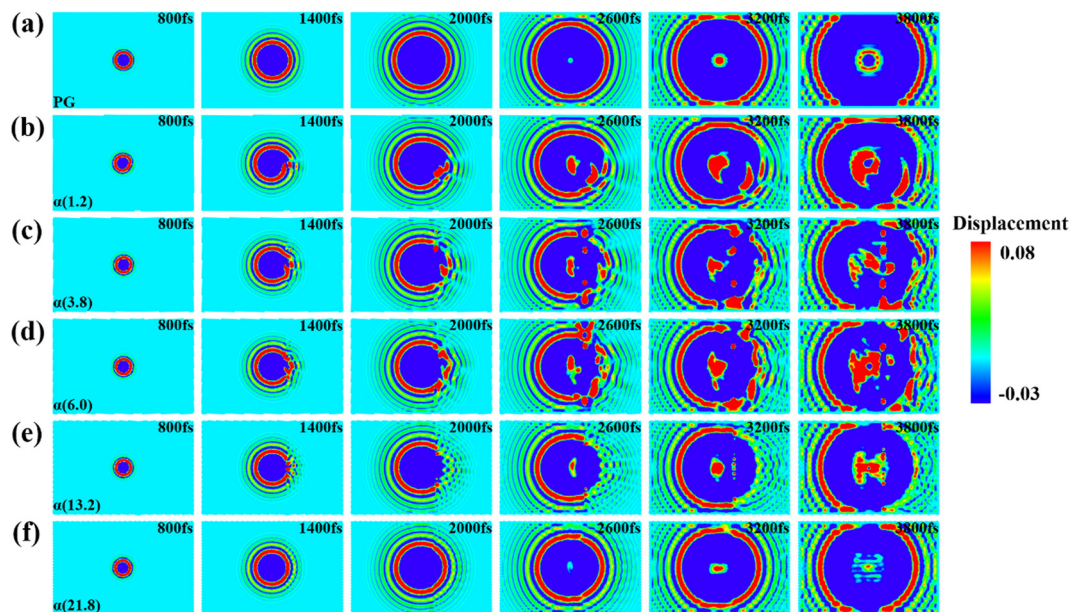
Fig. 3 Wrinkle propagation in PG and graphene with tilt GBs based on the impact from a C_{60} molecule. The distributions of the out-of-plane displacement in (a) PG, and graphene sheets with (b) $\alpha(1.2)$ GB, (c) $\alpha(3.8)$ GB, (d) $\alpha(6.0)$ GB, (e) $\alpha(13.2)$ GB, and (f) $\alpha(21.8)$ GB. Atomic snapshots are taken from 800 to 3800 fs with a time span of 600 fs. The units for displacement are Å. Atoms are color coded as red for the maximum and blue for the minimum.

$\alpha(21.8)$ GB) are provided, as the phenomenon of abnormal wrinkle propagation in graphene with tilt GBs can be sufficiently verified from the snapshots in Fig. 3b–f. The effect of the other tilt GBs ($\alpha(2.1)$ GB, $\alpha(5.0)$ GB, $\alpha(7.3)$ GB, and $\alpha(9.4)$ GB) on wrinkle propagation are discussed based on the RMS in Fig. 6 and 8. The formation and propagation of impact-induced dynamic wrinkles are observed from the atomic-level simulations in Fig. 3. Atomic snapshots of the dynamic wrinkle propagation are obtained from 800 to 3800 fs with an interval of 600 fs.

Initially, a C_{60} molecule moves towards the graphene sheet at an initial vertical speed of 15 Å ps^{-1}. A slightly upward bubble appears at the center of the graphene due to the attractive force between the C_{60} molecule and graphene. As the impact continues, the center of the graphene moves downward to form a cone, and dynamic wrinkle propagation occurs. For PG, from 800 to 2000 fs in Fig. 3a, relatively regular circular wrinkles spread toward the fixed edges. The smooth wrinkles reflect from the upper and lower boundaries and interference is observed (see snapshots from 2600 to 3800 fs in Fig. 3a). Meanwhile, the center of graphene vibrates near the initial equilibrium position and forms more circular wrinkles after 3200 fs.

For defective graphene, before arriving at the tilt GBs, the dynamic wrinkles propagate in the form of approximate circles (see 800 fs in Fig. 3b–f). The dynamic wrinkles exhibit irregular and discontinuous types of behavior after crossing through tilt GBs (see snapshots from 2000 to 3800 fs in Fig. 3b–d). There usually exists a shielding effect from defects on dynamic wrinkle propagation in graphene, as verified in our previous study.[50] In general, an increased misorientation angle α causes

the number N of 5–7 defects to increase, which may lead to more dramatic diffraction and interference. Therefore, the shielding effect of GBs on dynamic wrinkles can become more significant with an increased N. However, the dynamic wrinkles are smooth and regular after crossing through the $\alpha(13.2)$ and $\alpha(21.8)$ GBs (see Fig. 3e and f).

These results further prove that dynamic wrinkles can be used to detect the defect type based on different out-of-plane configurations, which has been used in other studies.[14,50] Moreover, this counterintuitive phenomenon reveals an anomalous effect of the tilt GBs on dynamic wrinkle propagation. Morphologically, the dynamic circular wrinkles are incomplete with smaller α (see Fig. 3b–d) and become complete as the misorientation angle α increases (see Fig. 3e and f). This indicates that the shielding effect of tilt GBs on dynamic wrinkles can be enhanced before it is weakened, as the misorientation angle α increases. To explain this anomalous phenomenon, the out-of-plane displacement of seven special atoms (Fig. 4), the evolution of GB line configurations (Fig. 5), and the RMS values of the out-of-plane displacement for different atomic regions (Fig. 6a–c) are monitored during the simulations.

The out-of-plane displacements of seven special atoms were monitored to study the effect of tilt GBs on wrinkle propagation. Generally, the out-of-plane displacements of special atoms can provide an intuitive understanding of the evolution of dynamic wrinkles.[14,16,50] Moreover, these values can be used to calculated the speed of dynamic wrinkle propagation.[15] Fig. 4 shows the time history of the out-of-plane displacement of these seven atoms (atom-a, atom-b, atom-c, atom-d, atom-e, atom-f, and atom-g) in PG and graphene with five tilt GBs ($\alpha(1.2)$ GB, $\alpha(3.8)$ GB, $\alpha(6.0)$ GB,

3684 | *Phys. Chem. Chem. Phys.*, 2023, **25**, 3681–3694
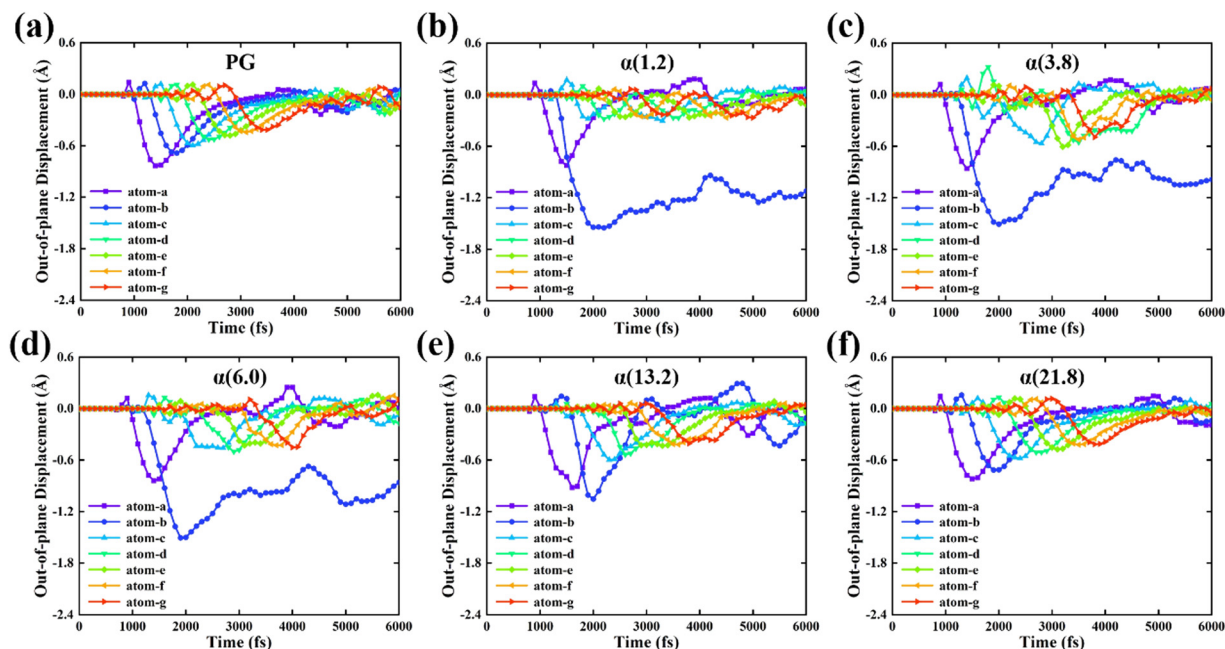
This journal is © the Owner Societies 2023

Fig. 4 Time history of the out-of-plane displacements for seven atoms (atom-a, atom-b, atom-c, atom-d, atom-e, atom-f, and atom-g) in (a) PG, and graphene with (b) α(1.2) GB, (c) α(3.8) GB, (d) α(6.0) GB, (e) α(13.2) GB, and (f) α(21.8) GB.

α(13.2) GB, and α(21.8) GB). As there exists a 10 Å initial vertical gap between graphene and the C_{60} molecule, out-of-plane displacement can remain constant until the C_{60} molecule moves into the interactive distance regime and dynamic wrinkles appear at the first monitoring point. The amplitudes of the monitored points decrease gradually with the propagation of the dynamic wrinkles in PG (see Fig. 4a), which is attributed to fast exponential damping.[14] Usually, the amplitudes of these atoms in defective graphene sheets present irregularity due to fluctuations caused by out-of-plane buckling of the 5–7 defects.

Specifically, the relaxation strategy in Section 2.2 indicates that the maximum z-direction displacements of atom-a are 0.83, 0.82, 0.86, 0.84, 0.92, and 0.82 Å (see Fig. 4a–f). Unlike PG, the maximum out-of-plane displacements of atom-b are greater than those of atom-a in graphene, with α(1.2) GB, α(3.8) GB, α(6.0) GB, and α(13.2) GB (see Fig. 4b–e) at 0.69, 1.55, 1.51, 1.51, 1.05, and 0.71 Å, respectively (see Fig. 4a–f). The amplitudes of atom-b can be nearly twice those of atom-a in graphene with α(1.2) GB, α(3.8) GB, and α(6.0) GB. Slight fluctuations in atom-b around the secondary equilibrium position are observed after 3000 fs (see Fig. 4b–d). For PG and graphene with α(13.2) GB and α(21.8) GB, atom-b tends to vibrate around the initial equilibrium position after 3000 fs (see Fig. 4a, e and f).

As illustrated in Fig. 4f, all monitored points in graphene with α(21.8) GB exhibit regular fluctuations that are similar to the evolution of the PG curves (Fig. 4a), which is unexpected and counterintuitive since the fluctuating GB atoms can be more drastic with more 5–7 defects. This unexpected result indicates that the out-of-plane deformation of the GB region increases first and then decreases with the 5–7 defect density. This result also implies that the dense 5–7 defects in graphene

with the α(21.8) GB can counteract the effect of tilt GBs on wrinkle propagation. The mutual constraint and interaction of out-of-plane fluctuations between adjacent 5–7 defects could be responsible for this result.[54] Moreover, the evolution of out-of-plane displacements for atom-b implies that energy from the impact can be absorbed by GBs and converted to their out-of-plane deformation energy. Therefore, GB defects at small misorientation angles α could absorb and store energy from dynamic wrinkles but be less capable of secondary spreading of the attained energy.[14,19,50] This characteristic provides a theoretical basis for the defect engineering design of energy-absorbing devices and protectors at the nanoscale.

To further verify the accuracy of the simulation methods, the dynamic wrinkle propagation velocity ν_{w} can be obtained from[60]

$$\nu_{w} \approx Ca_0 \left\{ \frac{\nu_{initial}}{a_0\sqrt{2}} \right\}^{\frac{2}{3}} \qquad (1)$$

where C is a constant of 1.23, a_0 represents the longitudinal dynamic speed and is equal to 222 Å ps^{-1},[15] and $\nu_{initial}$ is the initial velocity of the C_{60} molecule at 15 Å ps^{-1}. The analytical solution of the dynamic wrinkle velocity can be calculated from eqn (1) as 35.95 Å ps^{-1}. In the MD simulations, the dynamic wrinkle velocities are calculated by dividing the adjacent point distance by the arrival time (see Fig. 4), and the calculation results are approximately constant. The average velocity for PG is 32.82 Å ps^{-1}, and that for defective graphene with different GBs of α(1.2), α(3.8), α(6.0), α(13.2), and α(21.8) GBs is approximately 33.53, 32.77, 32.84, 32.81, and 33.74 Å ps^{-1}, respectively. The results show a small difference between the PG and
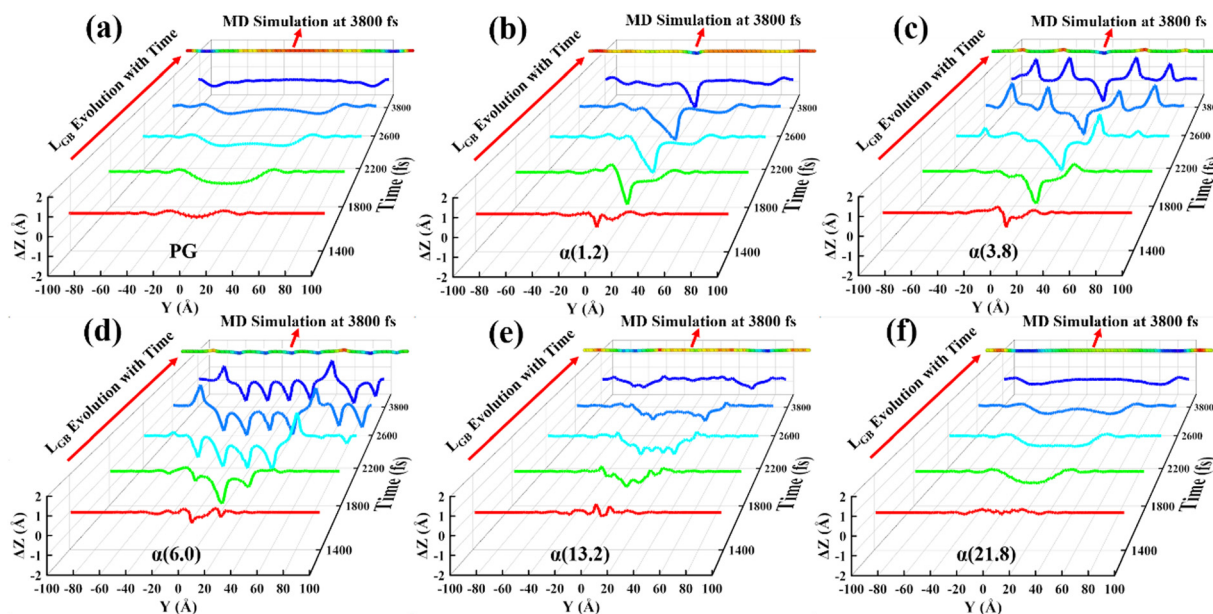
Fig. 5 Evolution of the out-of-plane configuration for L_{GB} at 1400, 1800, 2200, 2600, and 3800 fs. Configuration evolution of L_{GB} in (a) PG, and graphene sheets with (b) α(1.2) GB, (c) α(3.8) GB, (d) α(6.0) GB, (e) α(13.2) GB, and (f) α(21.8) GB.

defective graphene, which is attributed to the slight contraction of the defective graphene due to relaxation. There is a good agreement between the theoretical and MD methods, which implies that the MD simulations are reliable.

The evolution of out-of-plane deformation for L_{GB} is obtained to better understand the effect of the GB region on dynamic wrinkle propagation. Fig. 5 shows the time history of Δz (the out-of-plane displacement) for L_{GB} in the PG and defective graphene samples with α(1.2) GB, α(3.8) GB, α(6.0) GB, α(13.2) GB, and α(21.8) GB. The MD simulations of L_{GB} atoms at 3800 fs provide an intuitive comparison with the plotted configurations. As time progresses, the apparent out-of-plane configurations of L_{GB} are observed. The middle part of each configuration presents a downward trend at 1400 fs. For PG, the evolution of the configuration is smooth and symmetric during the entire simulation (see Fig. 5a). For graphene with α(1.2) GB, α(3.8) GB, α(6.0) GB, and α(13.2) GB, sharp bulges indicate that buckling of the middle defects in GBs occurs due to strikes from the dynamic wrinkles (see 1400 fs in Fig. 5b–e).

With the propagation of dynamic wrinkles, more bulges are observed, and the number of bulges is the same as the number of 5–7 defects. After 2600 fs, significant and stable out-of-plane configurations of L_{GB} are observed in Fig. 5b–d. However, for PG and graphene with α(13.2) GB and α(21.8) GB, atoms in the GB regions tend to fluctuate around the initial equilibrium position (Fig. 5a, e and f). Compared with the strong local buckling of defects in Fig. 5b–d, the out-of-plane configurations of PG and graphene with α(21.8) GB exhibit a global bucking mode (see Fig. 5a and f), while Fig. 5e shows two mixed buckling modes. Generally, the direction of local buckling seems random, but the buckling direction of the central defect tends to be downward as the downward cone wrinkle propagation provides the initial perturbation. These results show that

the interactions between defects can be enhanced to reduce their out-of-plane displacements as the number of 5–7 defects increases. This provides further compelling evidence for the anomalous propagation of dynamic wrinkles in graphene with tilt GBs.

The out-of-plane displacements of special atoms and atomic lines can be random in a single direction, which cannot provide a full insight into dynamic wrinkle propagation. Thus, the RMS values of out-of-plane displacements for atomic regions are monitored to investigate the effect of tilt GBs on wrinkle propagation in the atomic regions.[50] The RMS values of the out-of-plane displacements for the R_{GB} and R_{80} are calculated to fully investigate the abnormal effects of tilt GBs on dynamic wrinkle propagation. Fig. 6a and b illustrate the time history of the Δz RMS values for the R_{GB} and R_{80} in PG and in graphene with α(1.2) GB, α(3.8) GB, α(6.0) GB, α(13.2) GB, and α(21.8) GB, and Fig. 6c plots the associated maximum RMS values. Fig. 6d shows the maximum out-of-plane displacement for the defects of all GBs during the simulations. The typical RMS displacements are calculated through the relationship:

$$\text{RMS} = \sqrt{\frac{\sum_{i=1}^{n} \Delta z_i^2}{n}} \qquad (2)$$

where Δz_i and n are the out-of-plane displacement and number of atoms in the monitored regions, respectively. As plotted in Fig. 6a, as the dynamic wrinkles propagate, the RMS values for the R_{GB} increase before 2000 fs and then decrease to relatively stable values. The maximum RMS values of the R_{GB} for the six graphene sheets are 0.35, 0.60, 0.60, 0.80, 0.42, and 0.33 Å, and the relatively stable values are approximately 0.13, 0.40, 0.61, 0.62, 0.14, and 0.13 Å, respectively. Comparing these values
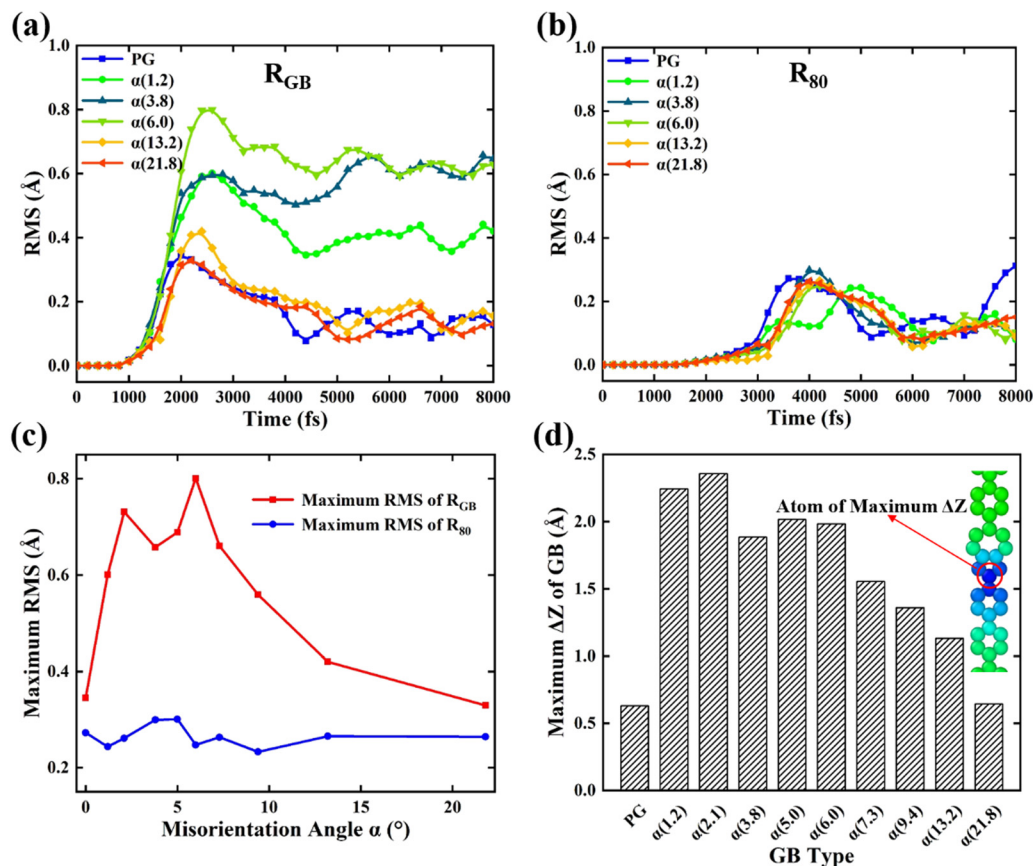
3686 | *Phys. Chem. Chem. Phys.*, 2023, **25**, 3681–3694

This journal is © the Owner Societies 2023

Fig. 6 Time history of the Δz RMS values for the (a) R_{GB} and (b) R_{80}, (c) evolution of the maximum RMS with respect to the GB misorientation angle α, and (d) maximum Δz of GBs in the different GB types.

indicates that the $\alpha(1.2)$ GB, $\alpha(3.8)$ GB, and $\alpha(6.0)$ GB have the capability of absorbing and storing energy from dynamic wrinkles. However, the curves for the $\alpha(13.2)$ GB and $\alpha(21.8)$ GB show a similar tendency as the PG since they could not readily absorb energy but could spread it. This result provides a theoretical foundation for the application of tilt GBs in the shielding effect of defects on wrinkle propagation.

Two factors affect the RMS values of the R_{GB}: the number of 5–7 defects, and the mutual constraint of out-of-plane deformations between neighboring defects. As the number of 5–7 defects increases, the RMS value of the R_{GB} also increases. However, interactions between neighboring defects can become stronger as the density of 5–7 defects increases, which leads to a reduced out-of-plane deformation in the GB region. Thus, the mutual interactions of two factors lead to the anomalous propagation of dynamic wrinkles in graphene with tilt GBs.

Fig. 6b shows the evolution of the RMS values for the R_{80}. Before 2000 fs, the plots are nearly constant, and there is a sharp increase from 2000 to 4000 fs with a peak around 4000 fs. The maximum RMS values of the R_{GB} for the six graphene sheets are 0.27, 0.24, 0.30, 0.25, 0.26, and 0.26 Å from $\alpha(1.2)$ GB to $\alpha(21.8)$ GB, respectively. The values of $\alpha(1.2)$ GB and $\alpha(6.0)$ are smaller than that of PG. However, the value of $\alpha(3.8)$ GB is greater, which is associated with the thermal fluctuation and

more buckling areas of the defect region than at the other GBs. The maximum RMS values of the R_{GB} and R_{80} for all GBs are plotted in Fig. 6c. In general, as the misorientation angle α increases, the maximum RMS of the R_{GB} increases first and then decreases, while the maximum RMS of the R_{80} shows the opposite trend. However, the RMS values of graphene with the $\alpha(3.8)$ GB and $\alpha(5.0)$ GB deviate from this trend, which is attributed to the interactions of neighboring defects and wrinkle reflection at fixed boundaries.

Fig. 6d illustrates the maximum out-of-plane displacements for all GBs. There is a sharp jump from the PG to graphene with the $\alpha(1.2)$ GB. The maximum displacement of graphene with $\alpha(1.2)$ GB is nearly the same as graphene with the $\alpha(2.1)$ GB at approximately 2.3 Å. Then, a slight decrease occurs in graphene with the $\alpha(3.8)$ GB. The maximum value decreases gradually from graphene with the $\alpha(5.0)$ GB to that with the $\alpha(21.8)$ GB. This indicates that the mutual constraint between neighboring defects occurs from graphene with $\alpha(5.0)$ GB. It is noted that the atom for the maximum out-of-plane displacement is the joint atom between the pentagonal and hexagonal carbon rings (see the red circle in Fig. 6d). The results in Fig. 6 provide additional evidence of anomalous dynamic wrinkle propagation in graphene with tilt GBs.

Various energy variations with respect to time are obtained through the MD simulations to provide energetic insight into

the dynamic wrinkle propagation in graphene with tilt GBs. Fig. 7a–d plot the time histories of the C_{60} kinetic energy as well as the average variation in the potential energy per atom for the graphene sheets and the R_{GB} and R_{80}, respectively. Fig. 7a describes the evolution of the C_{60} kinetic energy in PG and graphene with the $\alpha(1.2)$ GB, $\alpha(3.8)$ GB, $\alpha(6.0)$ GB, $\alpha(13.2)$ GB, and $\alpha(21.8)$ GB. The initial kinetic energy of C_{60} is 8.4 eV. There are fluctuations from the initial time through 400 fs due to the attractive and repulsive forces between C_{60} and graphene. Then, a sharp decrease occurs from 400 to 800 fs due to van der Waals interactions. After that, a slight increase is observed from 800 to 1200 fs, which indicates that C_{60} bounces off the lowest position. The C_{60} molecule is kept in a state of dynamic equilibrium with a kinetic energy of approximately 0.3 eV after 2000 fs. This implies that about 96% of the C_{60} kinetic energy is converted to kinetic and potential energies in graphene sheets. These results indicate that graphene is an excellent material for energy absorption, which can be used to design protectors and energy absorbers.[14,50] Snapshots of MD simulations from 0 to 6000 fs are obtained to help intuitively understand the C_{60} movement during the simulations.

Fig. 7b presents the variation in the potential energy per atom for PG and graphene with the $\alpha(1.2)$ GB, $\alpha(3.8)$ GB, $\alpha(6.0)$ GB, $\alpha(13.2)$ GB, and $\alpha(21.8)$ GB. Two evolution modes are obtained. For PG, variations in the potential energy increase sharply from the initial time to 800 fs due to the rapid conversion of the C_{60} kinetic energy. Then, the average atomic

potential energy fluctuates slightly around 0.0006 eV. For defective graphene, variations in the potential energy per atom decrease sharply from the initial time to 1000 fs and then finally remain nearly constant. The difference between these two evolution modes is attributed to the relaxation strategy described in Section 2.2.

Variations in the potential energy per atom for the R_{GB} and R_{80} are illustrated in Fig. 7c and d, respectively. For PG, variations in the potential energy per atom for the R_{GB} and R_{80} fluctuate around 0 eV as carbon atoms vibrate around the initial equilibrium position. For defective graphene, there is an obvious decrease over the initial 400 fs. Then, the variation in the potential energy per atom fluctuates slightly due to conversions between kinetic and potential energies. As shown in Fig. 7c, the $\alpha(3.8)$ GB shows a greater variation in the potential energy per atom due to thermal fluctuations and mutual interactions from neighboring defects. Except for the $\alpha(1.2)$ GB, the variation in the potential energy per atom for defective graphene in Fig. 7d is close for the other GBs after 1000 fs. This is probably because of energy dissipation due to fast damping as an exponential function.

3.2. Effect of the distance d_1 on wrinkle propagation

To holistically understand the effects of the impact position on wrinkle propagation, MD simulations were performed to obtain phase diagrams of the maximum displacement RMS value for graphene with all tilt GBs from Fig. 1c. Fig. 8 shows contour
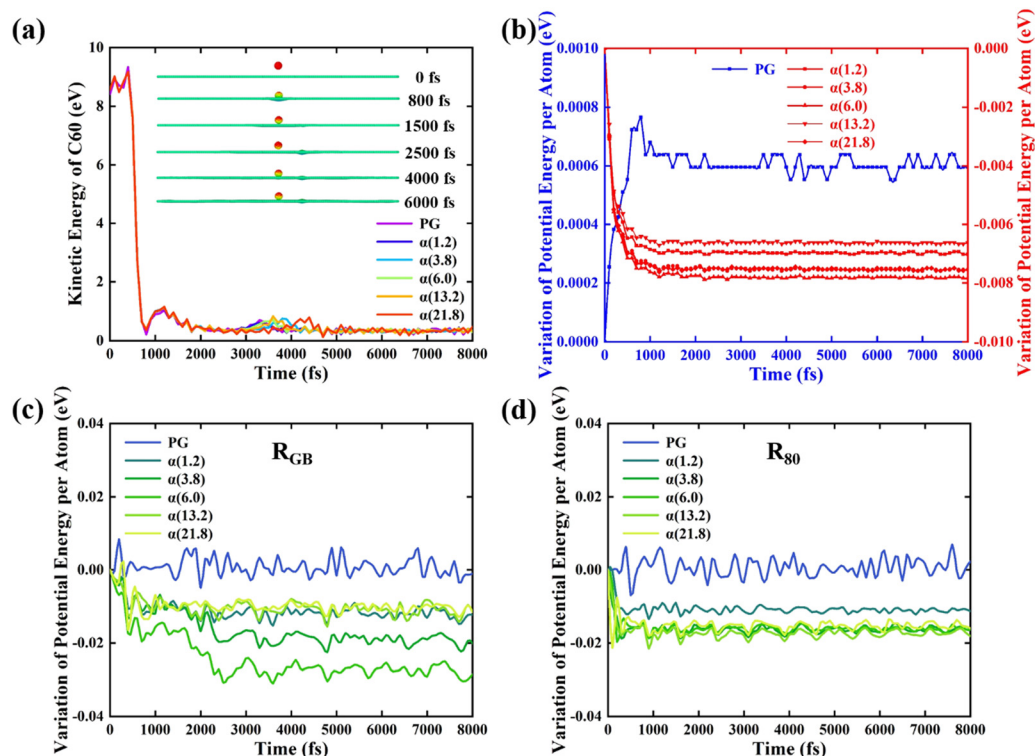

Fig. 7 Time history of energy variations from the MD simulations. (a) Time history of the C_{60} kinetic energy, (b) average variation in the potential energy per atom *versus* time for PG and graphene sheets with the $\alpha(1.2)$ GB, $\alpha(3.8)$ GB, $\alpha(6.0)$ GB, $\alpha(13.2)$ GB and $\alpha(21.8)$ GB; and average variation in the potential energy per atom *versus* time in the (c) R_{GB} and (d) R_{80}.

3688 | *Phys. Chem. Chem. Phys.*, 2023, **25**, 3681–3694

This journal is © the Owner Societies 2023

plots of the maximum displacement RMS in the parameter space of the distances d_1 and d_2. For convenient simulations and calculations, the tilt GBs are constructed in the middle of the graphene sheets. The peak values of the maximum RMS in Fig. 8a–i are 0.36, 0.35, 0.36, 0.37, 0.38, 0.39, 0.34, 0.37, and 0.37 Å from $\alpha(1.2)$ GB to $\alpha(21.8)$ GB, respectively. The peak values occur at (d_1, d_2) and are equal to (20, 20), (20, 20), (0, 20), (0, 20), (0, 20), (0, 20), (0, 20), (0, 20), and (0, 20), respectively. In general, as the distances d_1 and d_2 increase, the maximum RMS decreases due to fast exponential damping. As shown in Fig. 8a and g, the maximum RMS is just below 0.25 Å when $d_2 > 50$ Å. This implies that the RMS is more sensitive to the distance d_2.

Fig. 8b, e and h show that values on the left part of the phase diagrams are greater than those on the right, which indicates that the RMS is more sensitive to the distance d_1. The sensitivity of the maximum RMS in graphene with the $\alpha(3.8)$ GB, $\alpha(5.0)$ GB, $\alpha(7.3)$ GB, and $\alpha(21.8)$ GB to the distance d_1 is nearly the same as that for distance d_2, as evident from Fig. 8c, d, f, and i. For the $\alpha(21.8)$ GB, there is nearly no influence on the dynamic wrinkle propagation due to the strong mutual constraint of neighboring defects. The results in Fig. 8 provide direct and full insight into the influence of tilt GBs on dynamic wrinkle propagation. These results also help us understand the dynamic mechanical behavior of GBs in other 2D materials.

To comprehensively understand dynamic wrinkle propagation in graphene with tilt GBs, the out-of-plane displacement field at $d_1 = 0$ (i.e., the impact point at the middle of the GBs) can be obtained from MD simulations. The special formation and propagation of dynamic wrinkles is illustrated in Fig. 9 based on mapping the out-of-plane displacement field and molecular contours over graphene sheets during impact. Compared with the simulations in Fig. 3, the impact region is inhomogeneous when $d_1 = 0$, and the patterns of wrinkle propagation can differ. When $d_1 \neq 0$, the dynamic wrinkles can cross through the tilt GBs, and the local configuration of dynamic wrinkles can be influenced by them, as evident from Fig. 3. However, when $d_1 = 0$, the initial dynamic wrinkle occurs directly at the tilt GB region. The global configuration of dynamic wrinkle propagation is affected by tilt GBs. Therefore, the impact simulation initially shows that the defect region has upward buckling when undergoing perturbation caused by attractive forces between C_{60} and GBs, which leads to irregular circular propagation (see 800 fs in Fig. 9a–e). Dynamic wrinkle propagation cannot be affected by fluctuations of other defects as only one 5–7 defect exists in graphene with the $\alpha(1.2)$ GB.
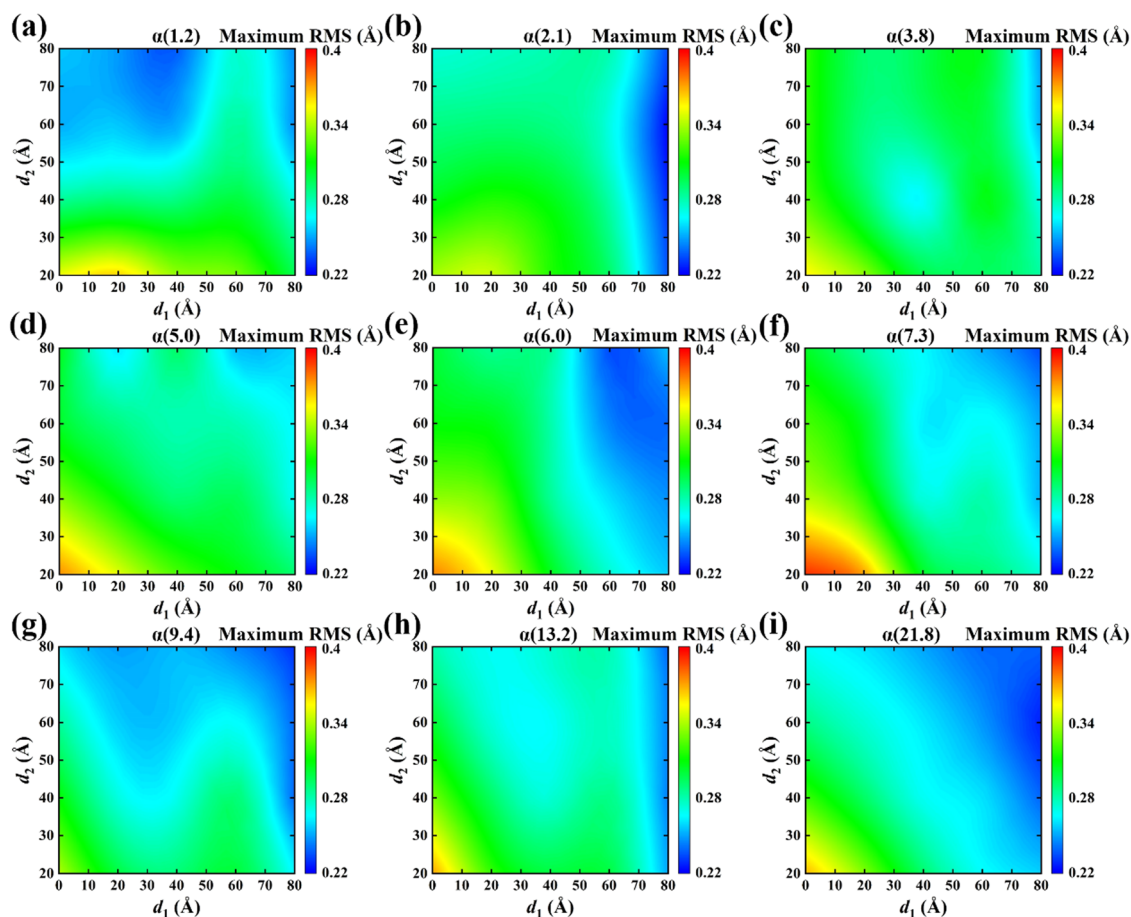

Fig. 8 Contour plots of the maximum RMS values in the parameter space of d_1 and d_2 for graphene sheets with the (a) $\alpha(1.2)$ GB, (b) $\alpha(2.1)$ GB, (c) $\alpha(3.8)$ GB, (d) $\alpha(5.0)$ GB, (e) $\alpha(6.0)$ GB, (f) $\alpha(7.3)$ GB, (g) $\alpha(9.4)$ GB, (h) $\alpha(13.2)$ GB, and (i) $\alpha(21.8)$ GB.
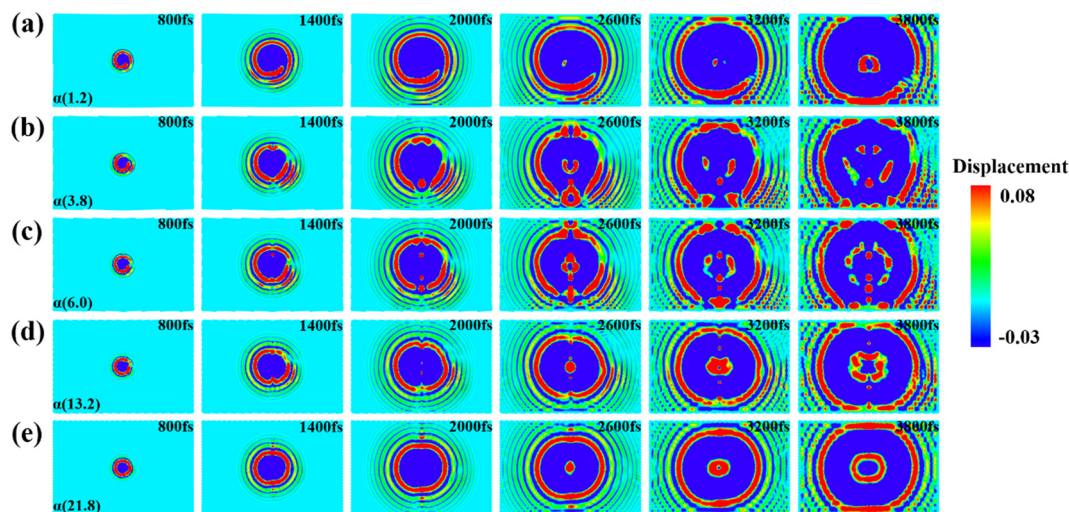
This journal is © the Owner Societies 2023

Phys. Chem. Chem. Phys., 2023, **25**, 3681–3694 | **3689**

Fig. 9 Wrinkle propagation in graphene sheets with five tilt GBs at $d_1 = 0$. The distributions of the out-of-plane displacement in the graphene sheets with the (a) $\alpha(1.2)$ GB, (b) $\alpha(3.8)$ GB, (c) $\alpha(6.0)$ GB, (d) $\alpha(13.2)$ GB, and (e) $\alpha(21.8)$ GB. The atomic snapshots are taken from 800 to 3800 fs with a time span of 600 fs.

The wrinkle propagation contour is a relatively regular but incomplete circle in Fig. 9a. The incompleteness of the contour is affected by inhomogeneous out-of-plane deformation from the middle defect. Fig. 9b–d show that the circular contours are divided into two semi-circles by the GB region due to the out-of-plane buckling at the defect region. The contours in Fig. 9e are oblate circles, which can contribute to the impeded wrinkle propagation from tilt GBs. Compared with the results in Fig. 3, the global completeness of the configurations is better, which indicates that the distance d_1 is an important factor in the formation and propagation of dynamic wrinkles. This figure, together with Fig. 3 and 8, reveals the effect of the distance d_1 on dynamic wrinkle propagation, which provides a theoretical basis for the application of defect engineering in dynamic wrinkle-free nanodevices.[14,19]

van der Waals interactions are usually used to describe the interaction of nanoparticles or the interlayer interaction of nano materials, which can provide further insight into impact dynamics.[12,61] The interactive forces between the C_{60} molecule and graphene sheets at $d_1 = 0$ and $d_1 = 30$ are presented in Fig. 10. During the impact simulations, the interactive force increases sharply and then decreases rapidly. The curves then fluctuate slightly around 0 nN, which indicates the C_{60} molecule vibrates with the graphene sheet. Specifically, a slight decline occurs at 400 fs due to the attractive force between the C_{60} molecule and graphene. As C_{60} is in its downward oscillation, the repulsive force can dominate and reaches a peak of approximately 5 nN at 800 fs. Then C_{60} bounces off the lowest position and the interaction decreases sharply to approximately -0.3 nN at 1400 fs. It is noted that there are several greater fluctuations after 1400 fs (see 2600 and 4000 fs in Fig. 10a and 4000 fs in Fig. 10b), which may contribute to reflections at the fixed boundaries and thermal fluctuations of the tilt GBs. The main trend of the curves for PG and defective graphene is consistent due to the homogeneous impact region, as illustrated in the inset in Fig. 10b. However, a snap-through
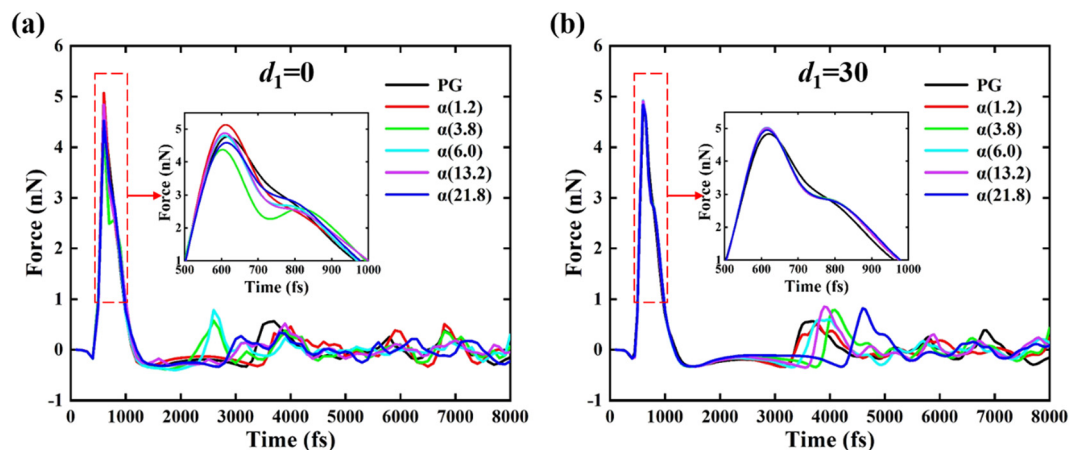

Fig. 10 Time history of the interactive force between the C_{60} molecule and graphene sheets at (a) $d_1 = 0$ and (b) $d_1 = 30$.
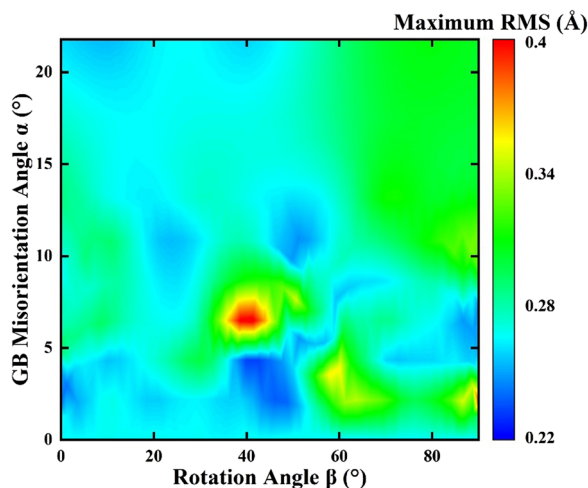
Fig. 11 Contour plots of the maximum RMS for the R_{60} in the parameter space of the rotation angle β and GB misorientation angle α at $d_1 = 30$ Å.

of the curve for the $\alpha(3.8)$ GB is observed in the inset of Fig. 10a. This indicates that the atomic structure around the defect suddenly becomes concave down, which leads to an abrupt but slight decrease in the repulsive force.

3.3. Influence of the rotation angle β on wrinkle propagation

To provide additional insight into the influence of the rotation angle β on wrinkle propagation, 100 simulation cases were performed to obtain the maximum RMS phase diagram of the R_{60} (*i.e.*, $d_2 = 30$ Å) in the parameter space of the rotation angle β and the GB misorientation angle α at $d_1 = 30$ Å, as plotted in Fig. 11. As the rotation angle β increases, the maximum RMS value increases. With an increased GB misorientation angle α, the maximum RMS increases first and then decreases, which coincides with the results in Fig. 6. The maximum RMS occurs at $(\alpha, \beta) = (6.0°, 40°)$ at 0.43 Å. There are two reasons for variations in the maximum RMS. On the one hand, the increased rotation angle β may increase the number of 5–7 defects in

defective graphene. This usually leads to more out-of-plane deformations in the monitored region R_{60}. On the other hand, it is important to identify whether or not the additional defects are located at the monitored region R_{60}. When additional defects are observed near or at the monitored region, the maximum RMS value can increase.

Fig. 12 shows snapshots of wrinkle propagation at different rotation angles for five defective graphene samples. The initial vertical distance d_1 is 30 Å when $\beta = 0°$. As the rotation angle β varies, the vertical distance between the impact point and the tilt GBs is calculated from the expression $30\cos\beta$. Thus, the impact point is at the GB region when $\beta = 90°$. Generally, the configurations in Fig. 12 are similar to those in Fig. 3 at smaller rotation angles (see $\beta = 30°$ in Fig. 12). The contours of dynamic wrinkle propagation in graphene with the $\alpha(13.2)$ GB and $\alpha(21.8)$ GB (see Fig. 12d and e, respectively) are consistent with those in Fig. 4e and f due to the smaller out-of-plane buckling defects. Specifically, as dynamic wrinkles propagate, the defect buckling near the impact point occurs first. Defect buckling near the impact point under dynamic wrinkle propagation provides the perturbation that leads to the buckling of defects far from the impact point (see 200 fs at $\beta = 60°$ in Fig. 12a–c). The 5–7 defects in GBs are considered as the second-generation fluctuation source, which leads to interference (see $\beta = 60°$ and $\beta = 90°$ in Fig. 12a–c). The propagation direction of dynamic wrinkles can also be changed by the interference (see 4800 fs at $\beta = 60°$ and $\beta = 90°$ in Fig. 12a–c). The results obtained in Fig. 12 offer important insight to further understand tilt GBs for wrinkle propagation.

4. Conclusions

Atomistic simulations were conducted to study dynamic wrinkle propagation in polycrystalline graphene with tilt GBs. Anomalous wrinkle propagation is observed through snapshots of the out-of-plane displacement. This counterintuitive phenomenon reveals the shielding effect of tilt GBs on dynamic
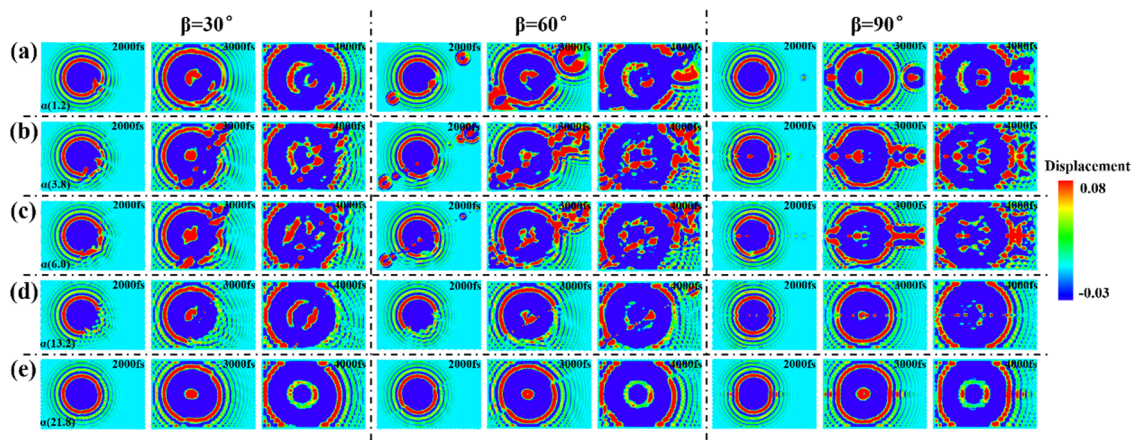

Fig. 12 Wrinkle propagation in defective graphene sheets with different rotation angles ($\beta = 30°$, $60°$, and $90°$) at $d_1 = 30$ Å. Distributions of the out-of-plane displacement in the graphene sheets with the (a) $\alpha(1.2)$ GB, (b) $\alpha(3.8)$ GB, (c) $\alpha(6.0)$ GB, (d) $\alpha(13.2)$ GB, and (e) $\alpha(21.8)$ GB. Atomic snapshots are taken at 2000, 3000, and 4000 fs.

wrinkles, which can be enhanced and then weakened with an increasing misorientation angle α. The out-of-plane displacements of special atoms and the atomic line are monitored to reveal the local and global buckling modes of tilt GB regions. The theoretical value of the wrinkle propagation velocity is 35.95 Å ps^{-1}. The velocities from the MD simulations for PG and defective graphene with $\alpha(1.2)$, $\alpha(3.8)$, $\alpha(6.0)$, $\alpha(13.2)$, and $\alpha(21.8)$ GBs are 32.82, 33.53, 32.77, 32.84, 32.81, and 33.74 Å ps^{-1}, respectively, which agree well with the theoretical values. The maximum RMS values of out-of-plane displacements are calculated. As the misorientation angle α increases, the maximum RMS of the R_{GB} increases first and then decreases, while the maximum RMS value of the R_{80} exhibits the opposite trend. The evolution of the C_{60} kinetic energy and the average variation in the potential energy per atom for the graphene sheets and for the R_{GB} and R_{80} are investigated *via* MD simulations. Approximately 96% of the C_{60} kinetic energy is converted into kinetic and potential energies in graphene. The potential energy in graphene exhibits two evolution modes due to the proposed relaxation strategy. The phase diagrams of the maximum displacement RMS data for nine GBs are obtained to study the effect of the distance d_1 on wrinkle propagation. The figures show that the maximum RMS is more sensitive to the distance d_1 for the $\alpha(2.1)$ GB, $\alpha(6.0)$ GB, and $\alpha(13.2)$ GB but is less sensitive for the $\alpha(1.2)$ GB and $\alpha(9.4)$ GB. The interactive force between the C_{60} molecule and graphene is plotted, and a snap-through of the curve for $\alpha(3.8)$ GB is observed. Finally, 100 simulation cases are performed to study the influence of the rotation angle β on wrinkle propagation. The phase diagram shows that the maximum RMS value occurs at $(\alpha,\beta) = (6.0°,40°)$ at 0.43 Å. These results shed light on the fundamental understanding of defect engineering and on guidelines for the design of protectors, energy absorbers, and defect detectors in nanodevices.

Conflicts of interest

There are no conflicts of interest to declare.

Acknowledgements

References

1 K. S. Novoselov, A. K. Geim, S. V. Morozov, D. Jiang, Y. Zhang, S. V. Dubonos, I. V. Grigorieva and A. A. Firsov, Electric Field Effect in Atomically Thin Carbon Films, *Science*, 2004, **306**(5696), 666–669.

2 C. Lee, X. Wei, J. W. Kysar and J. Hone, Measurement of the Elastic Properties and Intrinsic Strength of Monolayer Graphene, *Science*, 2008, **321**(5887), 385–388.

3 P. Zhang, L. Ma, F. Fan, Z. Zeng, C. Peng, P. E. Loya, Z. Liu, Y. Gong, J. Zhang, X. Zhang, P. M. Ajayan, T. Zhu and J. Lou, Fracture toughness of graphene, *Nat. Commun.*, 2014, **5**, 3782.

4 B. Deng, Y. Hou, Y. Liu, T. Khodkov, S. Goossens, J. Tang, Y. Wang, R. Yan, Y. Du, F. H. L. Koppens, X. Wei, Z. Zhang, Z. Liu and A. H. Peng, Growth of Ultraflat Graphene with Greatly Enhanced Mechanical Properties, *Nano Lett.*, 2020, **20**(9), 6798–6806.

5 F. Withers, M. Dubois and A. K. Savchenko, Electron properties of fluorinated single-layer graphene transistors, *Phys. Rev. B: Condens. Matter Mater. Phys.*, 2010, **82**(073403), 1–4.

6 C. Feng, Z. Yi, L. F. Dumee, F. She, Z. Peng, W. Gao and L. Kong, Tuning micro-wrinkled graphene films for stretchable conductors of controllable electrical conductivity, *Carbon*, 2018, **139**, 672–679.

7 X. Xu, L. F. C. Pereira, Y. Wang, J. Wu, K. Zhang, X. Zhao, S. Bae, C. T. Bui, R. Xie, J. T. L. Thong, B. H. Hong, K. P. Loh, D. Donadio, B. Li and B. Özyilmaz, Length-dependent thermal conductivity in suspended single-layer graphene, *Nat. Commun.*, 2014, **5**, 3689.

8 A. A. Balandin, Thermal properties of graphene and nanostructured carbon materials, *Nat. Mater.*, 2011, **10**, 569.

9 S. Ghosh, I. Calizo, D. Teweldebrhan, E. P. Pokatilov, D. L. Nika, A. A. Balandin, W. Bao, F. Miao and C. N. Lau, Extremely high thermal conductivity of graphene: Prospects for thermal management applications in nanoelectronic circuits, *Appl. Phys. Lett.*, 2008, **92**(151911), 1–3.

10 C.-C. Hsu, M. L. Teagu, J.-Q. Wang and N.-C. Yeh, Nanoscale strain engineering of giant pseudo-magnetic fields, valley polarization, and topological channels in graphene, *Sci. Adv.*, 2020, **6**(eaat9488), 1–8.

11 P. Jia, W. Chen, J. Qiao, M. Zhang, X. Zheng, Z. Xue, R. Liang, C. Tian, L. He, Z. Di and X. Wang, Programmable graphene nanobubbles with three-fold symmetric pseudo-magnetic fields, *Nat. Commun.*, 2019, **10**(1), 3127.

12 S. Hosseini-Hashemi, A. Sepahi-Boroujeni and S. Sepahi-Boroujeni, Analytical and molecular dynamics studies on the impact loading of single-layered graphene sheet by fullerene, *Appl. Surf. Sci.*, 2018, **437**, 366–374.

13 J.-H. Lee, P. E. Loya, J. Lou and E. L. Thomas, Dynamic mechanical behavior of multilayer graphene via supersonic projectile penetration, *Science*, 2014, **346**(6213), 1089–1092.

14 Y. Dong, Y. He, Y. Wang and H. Li, A theoretical study of ripple propagation in defective graphene, *Carbon*, 2014, **68**, 742–747.

15 B. Z. G. Haque, S. C. Chowdhury and J. W. Gillespie Jr., Molecular simulations of stress wave propagation and perforation of graphene sheets under transverse impact, *Carbon*, 2016, **102**, 126–140.

16 L. Yang and L. Tong, Suspended monolayer graphene traps high-speed single-walled carbon nanotube, *Carbon*, 2016, **107**, 689–695.

3692 | *Phys. Chem. Chem. Phys.*, 2023, **25**, 3681–3694

This journal is © the Owner Societies 2023

17 K. Yoon, A. Ostadhossein and A. C. T. V. Duin, Atomistic-scale simulations of the chemomechanical behavior of graphene under nanoprojectile impact, *Carbon*, 2016, **99**, 58–64.

18 X. Liu, F. Wang and H. Wu, Anisotropic propagation and upper frequency limitation of terahertz waves in graphene, *Appl. Phys. Lett.*, 2013, **103**(071904), 1–4.

19 Z. Yang, F. Ma and K. Xu, Grain boundaries guided vibration wave propagation in polycrystalline graphene, *RSC Adv.*, 2017, **7**(40), 24667–24673.

20 P. Liu, Y. W. Zhang and H. J. Gao, Interior and Edge Elastic Waves in Graphene, *J. Appl. Mech.*, 2013, **80**(040901), 1–5.

21 J. Xia, Y. Zhu, F. Wang and H. Wu, Effect of grain boundaries on mechanical transverse wave propagations in graphene, *J. Appl. Phys.*, 2017, **121**(215105), 1–6.

22 C. G. Wang, L. Lan, Y. P. Liu and H. F. Tan, Defect-guided wrinkling in graphene, *Comp. Mater. Sci.*, 2013, **77**, 250–253.

23 C. Wang, Y. Liu, L. Lan and H. Tan, Graphene wrinkling: formation, evolution and collapse, *Nanoscale*, 2013, **5**, 4454–4461.

24 X. Liu, F. Wang and H. Wu, Anisotropic growth of buckling-driven wrinkles in graphene monolayer, *Nanotechnology*, 2015, **26**(065701), 1–8.

25 J. Varillas and O. Frank, Wrinkle development in graphene sheets with patterned nano-protrusions: A molecular dynamics study, *Carbon*, 2021, **173**, 301–310.

26 A. Smolyanitsky and V. K. Tewary, Manipulation of graphene's dynamic ripples by local harmonic out-of-plane excitation, *Nanotechnology*, 2013, **24**(055701), 1–8.

27 H. Wu and X. Liu, Tuning electromechanics of dynamic ripple pattern in graphene monolayer, *Carbon*, 2016, **98**, 510–518.

28 P. Y. Huang, C. S. Ruiz-Vargas, A. M. V. D. Zande, W. S. Whitney, M. P. Levendorf, J. W. Kevek, S. Garg, J. S. Alden, C. J. Hustedt, Y. Zhu, J. Park, P. L. McEuen and D. A. Muller, Grains and grain boundaries in single-layer graphene atomic patchwork quilts, *Nature*, 2011, **469**(7330), 389.

29 J. Wu, Y. Li, D. Pan, C. Jiang, C. Jin, F. Song, G. Wang and J. Wan, Effect of grain boundaries on charge transport in CVD-grown bilayer graphene, *Carbon*, 2019, **147**, 434–440.

30 G. G. Jernigan, B. L. VanMil, J. L. Tedesco, J. G. Tischler, E. R. Glaser, A. Davidson III, P. M. Campbell and D. K. Gaskill, Comparison of epitaxial graphene on Si-face and C-face 4H SiC formed by ultrahigh vacuum and RF furnace production, *Nano Lett.*, 2009, **9**(7), 2605–2609.

31 Y. Hernandez, V. Nicolosi, M. Lotya, F. M. Blighe, Z. Sun, S. De, I. T. McGovern, B. Holland, M. Byrne, Y. K. Gun'Ko, J. J. Boland, P. Niraj, G. Duesberg, S. Krishnamurthy, R. Goodhue, J. Hutchison, V. Scardaci, A. C. Ferrari and J. N. Coleman, High-yield production of graphene by liquid-phase exfoliation of graphite, *Nat. Nanotechnol.*, 2008, 3 (9), 563.

32 K. Saitoh and H. Hayakawa, Motion of a free-standing graphene sheet induced by the collision with an argon nanocluster: Analyses of the detection and heat-up of the graphene, *Phys. Rev. B: Condens. Matter Mater. Phys.*, 2010, **81**(115447), 1–7.

33 S. Chun, Y. Choi and W. Park, All-graphene strain sensor on soft substrate, *Carbon*, 2017, **116**, 753–759.

34 J. A. Baimova, S. V. Dmitriev, K. Zhou and A. V. Savin, Unidirectional ripples in strained graphene nanoribbons with clamped edges at zero and finite temperatures, *Phys. Rev. B: Condens. Matter Mater. Phys.*, 2012, **86**(035427), 1–8.

35 A. P. Kauling, A. T. Seefeldt, D. P. Pisoni, R. C. Pradeep, R. Bentini, R. V. B. Oliveira, K. S. Novoselov and A. H. C. Neto, The Worldwide Graphene Flake Production, *Adv. Mater.*, 2018, **30**(1803784), 1–6.

36 S. Kurasch, J. Kotakoski, O. Lehtinen, V. Skakalova, J. Smet, C. E. Krill, A. V. Krasheninnikov and U. Kaiser, Atom-by-atom observation of grain boundary migration in graphene, *Nano Lett.*, 2012, **12**(6), 3168–3173.

37 A. Zandiatashbar, G.-H. Lee, S. J. An, S. Lee, N. Mathew, M. Terrones, T. Hayashi, C. R. Picu, J. Hone and N. Koratkar, Effect of defects on the intrinsic strength and stiffness of graphene, *Nat. Commun.*, 2014, **5**, 3186.

38 J.-H. Chen, L. Li, W. G. Cullen, E. D. Williams and M. S. Fuhrer, Tunable Kondo effect in graphene with defects, *Nat. Phys.*, 2011, **7**(7), 535–538.

39 G. Zhang, H. Liu, Y. Chen, H. Qin and Y. Liu, Strength criterion of graphene GBs combining discrete bond strength and varied bond stretch, *J. Mech. Phys. Solids*, 2022, **169**(105080), 1–21.

40 Y. Hwangbo, C.-K. Lee, S.-M. Kim, J.-H. Kim, K.-S. Kim, B. Jang, H.-J. Lee, S.-K. Lee, S.-S. Kim, J.-H. Ahn and S.-M. Lee, Fracture characteristics of monolayer CVD-graphene, *Sci. Rep.*, 2014, **4**, 4439.

41 A. Nourbakhsh, M. Cantoro, T. Vosch, G. Pourtois, F. Clemente, M. H. V. D. Veen, J. Hofkens, M. M. Heyns, S. D. Gendt and B. F. Sels, Bandgap opening in oxygen plasma-treated graphene, *Nanotechnology*, 2010, **21**(43), 435203.

42 P. Z. Sun, M. Yagmurcukardes, R. Zhang, W. J. Kuang, M. Lozada-Hidalgo, B. L. Liu, H.-M. Cheng, F. C. Wang, F. M. Peeters, I. V. Grigorieva and A. K. Geim, Exponentially selective molecular sieving through angstrom pores, *Nat. Commun.*, 2021, **12**, 7170.

43 B. Zheng and G. X. Gu, Tuning the graphene mechanical anisotropy via defect engineering, *Carbon*, 2019, **155**, 697–705.

44 K. V. Bets, V. I. Artyukhov and B. I. Yakobson, Kinetically Determined Shapes of Grain Boundaries in Graphene, *ACS Nano*, 2021, **15**, 4893–4900.

45 J. Sun, Y. Guo, Q. Wang and Y. Kawazoe, Thermal transport properties of penta-graphene with grain boundaries, *Carbon*, 2019, **145**, 445–451.

46 T. Ma, Z. Liu, J. Wen, Y. Gao, X. Ren, H. Chen, C. Jin, X.-L. Ma, N. Xu, H.-M. Cheng and W. Ren, Tailoring the thermal and electrical transport properties of graphene films by grain size engineering, *Nat. Commun.*, 2017, **8**, 14486.

47 X. Sun, Z. Wang and Y. Q. Fu, Adsorption and diffusion of sodium on graphene with grain boundaries, *Carbon*, 2017, **116**, 415–421.

This journal is © the Owner Societies 2023

Phys. Chem. Chem. Phys., 2023, **25**, 3681–3694 | **3693**

48 T. Zhang, X. Li and H. Gao, Defects controlled wrinkling and topological design in graphene, *J. Mech. Phys. Solids*, 2014, **67**, 2–13.

49 L.-J. Yin, J.-B. Qiao, W.-X. Wang, Z.-D. Chu, K. F. Zhang, R.-F. Dou, C. L. Gao, J.-F. Jia, J.-C. Nie and L. He, Tuning structures and electronic spectra of graphene layers with tilt grain boundaries, *Phys. Rev. B: Condens. Matter Mater. Phys.*, 2014, **89**(20), 205410.

50 Z. Zhao, Y. Wang and C. Wang, A theoretical study of wrinkle propagation in graphene with flower-like grain boundaries, *Phys. Chem. Chem. Phys.*, 2021, **23**(20), 11917–11930.

51 R. Grantab, V. B. Shenoy and R. S. Ruoff, Anomalous Strength Characteristics of Tilt Grain Boundaries in Graphene, *Science*, 2010, **330**, 946–948.

52 X. Liu, F. Wang and H. Wu, Anomalous twisting strength of tilt grain boundaries in armchair graphene nanoribbons, *Phys. Chem. Chem. Phys.*, 2015, **17**(47), 31911–31916.

53 L. Yi, Z. Yin, Y. Zhang and T. Chang, A theoretical evaluation of the temperature and strain-rate dependent fracture strength of tilt grain boundaries in graphene, *Carbon*, 2013, **51**, 373–380.

54 A. Fox, U. Ray and T. Li, Strength of graphene grain boundaries under arbitrary in-plane tension, *Carbon*, 2019, **142**, 388–400.

55 S. Plimpton, Fast parallel algorithms for short-range molecular dynamics, *J. Comput. Phys.*, 1995, **117**, 1–19.

56 S. J. Stuart, A. B. Tutein and J. A. Harrison, A reactive potential for hydrocarbons with intermolecular interactions, *J. Chem. Phys.*, 2000, **112**(14), 6472–6486.

57 J. Wu and Y. Wei, Grain misorientation and grain-boundary rotation dependent mechanical properties in polycrystalline graphene, *J. Mech. Phys. Solids*, 2013, **61**(6), 1421–1432.

58 J. Zhang, J. Zhao and J. Lu, Intrinsic Strength and Failure Behaviors of Graphene Grain Boundaries, *ACS Nano*, 2012, **6**(3), 2704–2711.

59 M. Becton and X. Wang, Tailoring patterns of graphene wrinkles by circular torsion, *Appl. Surf. Sci.*, 2016, **363**, 13–20.

60 S. L. Phoenix and P. K. Porwal, A new membrane model for the ballistic impact response and V50 performance of multi-ply fibrous systems, *Int. J. Solids Struct.*, 2003, **40**(24), 6723–6765.

61 Z. Xue, G. Chen, C. Wang and R. Huang, Peeling and sliding of graphene nanoribbons with periodic van der Waals interactions, *J. Mech. Phys. Solids*, 2022, **158**(104698), 1–26.

3694 | *Phys. Chem. Chem. Phys.*, 2023, **25**, 3681–3694

This journal is © the Owner Societies 2023